JOURNAL OF GEOPHYSICAL RESEARCH, VOL. 105, NO. D3, PAGES 3955–3973, FEBRUARY 16, 2000

A polar stratospheric cloud parameterization for the global modeling initiative three-dimensional model and its response to stratospheric aircraft

D. B. Considine,[1,2] A. R. Douglass,[3] P. S. Connell,[4] D. E. Kinnison,[4,5] and D. A. Rotman[4]

Abstract. We describe a new parameterization of polar stratospheric clouds (PSCs) which was written for and incorporated into the three-dimensional (3-D) chemistry and transport model (CTM) developed for NASA's Atmospheric Effects of Aviation Project (AEAP) by the Global Modeling Initiative (GMI). The parameterization was designed to respond to changes in NO_y and H_2O produced by high-speed civilian transport (HSCT) emissions. The parameterization predicts surface area densities (SADs) of both Type 1 and Type 2 PSCs for use in heterogeneous chemistry calculations. Type 1 PSCs are assumed to have a supercooled ternary sulfate (STS) composition, and Type 2 PSCs are treated as water ice with a coexisting nitric acid trihydrate (NAT) phase. Sedimentation is treated by assuming that the PSC particles obey lognormal size distributions, resulting in a realistic mass flux of condensed phase H_2O and HNO_3. We examine a simulation of the Southern Hemisphere high-latitude lower stratosphere winter and spring seasons driven by temperature and wind fields from a modified version of the National Center for Atmospheric Research (NCAR) Middle Atmosphere Community Climate Model Version 2 (MACCM2). Predicted PSC SADs and median radii for both Type 1 and Type 2 PSCs are consistent with observations. Gas phase HNO_3 and H_2O concentrations in the high-latitude lower stratosphere qualitatively agree with Cryogenic Limb Array Etalon Spectrometer (CLAES) HNO_3 and Microwave Limb Sounder (MLS) H_2O observations. The residual denitrification and dehydration of the model polar vortex after polar winter compares well with atmospheric trace molecule spectroscopy (ATMOS) observations taken during November 1994. When the NO_x and H_2O emissions of a standard 500-aircraft HSCT fleet with a NO_x emission index of 5 are added, NO_x and H_2O concentrations in the Southern Hemisphere polar vortex before winter increase by up to 3%. This results in earlier onset of PSC formation, denitrification, and dehydration. Active Cl_y increases and produces small (~1%) decreases in lower stratospheric vortex O_3 concentrations during the spring relative to the HSCT-free run.

1. Introduction

The potential effects of a fleet of high-speed civilian transports (HSCTs) on the atmosphere have traditionally been evaluated using two-dimensional (2-D) models of stratospheric photochemistry and dynamics [*Stolarski et al.,* 1995]. These evaluations have been criticized primarily because 2-D models have highly parameterized descriptions of important atmospheric features such as the winter polar vortex. These models might therefore not respond to HSCT emissions in the same manner as the atmosphere, resulting in incorrect predictions of HSCT effects.

The Global Modeling Initiative (GMI) of NASA's Atmospheric Effects of Aviation Project (AEAP) was organized to respond to these concerns. Its goal is to create a three-dimensional (3-D) model capable of assessing the possible effects of aircraft on the atmosphere [*Rodriguez,* 1996]. Ultimately, a 3-D model should provide a better prediction of the impact of HSCT emissions than a 2-D model does, due to its more physically correct representation of some atmospheric processes.

[1]Earth System Science Interdisciplinary Center and Department of Meteorology, University of Maryland, College Park.

[2]Also at NASA Goddard Space Flight Center, Greenbelt, Maryland.

[3]NASA Goddard Space Flight Center, Greenbelt, Maryland.

[4]Lawrence Livermore National Laboratory, Livermore, California.

[5]Now at National Center for Atmospheric Research, Boulder, Colorado.

Copyright 2000 by the American Geophysical Union.

Paper number 1999JD900932.
0148-0227/00/1999JD900932$09.00

However, the use of 3-D models as assessment tools is still in its infancy. While the 3-D model created by the GMI participated in the most recent aircraft assessment conducted by the AEAP, its simulation of the natural atmosphere and its response to aircraft emissions are yet to be fully evaluated.

HSCT emissions will increase the amounts of H_2O and NO_x in the cold polar vortices, possibly increasing the frequency of occurrence of polar stratospheric clouds (PSCs). This could produce increased activation of chlorine and destruction of O_3 [*Peter et al.,* 1991; *Pitari et al.,* 1993; *Considine et al.,* 1994]. The PSC parameterization in a model designed to assess the effects of HSCT emissions must therefore respond realistically to those emissions. To be realistic, the PSC parameterization must consider the primary physical processes controlling the occurrence of PSCs, which include particle nucleation, condensation and evaporation, and sedimentation [*Peter,* 1997; *Turco et al.,* 1989]. However, 3-D models demand more computer resources than do 2-D models, due to a larger number of model grid points and (typically) time steps during the day. It is currently not practical to treat PSC processes in a 3-D assessment model using a sophisticated particle size-resolving microphysical treatment such as that of *Pitari et al.* [1993] or *Larsen* [1991].

In this paper we describe the PSC parameterization written for and implemented in the GMI model. It responds to HSCT emissions and considers the PSC processes mentioned above in a relatively simple and straightforward way. We show that with this parameterization the model simulation of the polar winter and spring lower stratosphere compares reasonably well with observations. We focus in particular on the predicted denitrification and dehydration of the polar vortex, which has received little attention in previous studies. We then present the response of the model Southern Hemisphere to the addition of HSCT emissions.

Section 2 briefly describes the version of the GMI 3-D chemistry and transport model (CTM) used in this study. Section 3 outlines the PSC parameterization in detail. Section 4 discusses the data used to evaluate the model performance. Section 5 sketches the model runs conducted for this study. Section 6 examines the model output in some detail and compares it with observations. Section 7 characterizes the response of the model Southern Hemisphere high-latitude region to aircraft emissions. A summary and some conclusions are then presented in section 8.

2. The GMI 3-D CTM

The GMI 3-D CTM will be described in detail in a forthcoming publication (D. Rotman et al., manuscript in preparation, 1999). Here we present a brief description which is sufficient for the purpose of this paper. The model was designed with the idea that it would be the primary tool of a science team organized to investigate the aircraft emissions problem. It is thus configured to facilitate swapping of program modules which might have similar functions but different formulations, allowing easy testing and intercomparison. Modules are contributed by science team members and are incorporated into the model by a core group of scientists who are currently at the Lawrence Livermore National Laboratory. For instance, three different chemical integrators were tested in the model, including SMVGEAR II [*Jacobson,* 1995], and two fast solvers [*Ramarosen et al.,* 1992; *Granier and Brasseur,* 1991]. The relative simplicity of changing chemical integrators allowed the use of SMVGEAR II as a standard against which the others could be evaluated in an "operational" setting (P. S. Connell et al., manuscript in preparation, 1999).

Three sources of the meteorological data used to drive the model are available: (1) the Goddard Space Flight Center (GSFC) Goddard Earth Observing System (GEOS-1) Data Assimilation System [*Schubert et al.,* 1993], (2) the Goddard Institute for Space Studies General Circulation Model II′ (GISS II′) [*Koch and Rind,* 1998], and (3) a modified version of the National Center for Atmospheric Research (NCAR) Middle Atmosphere Community Climate Model Version 2 (MACCM2) [*Boville,* 1995]. In all cases constituents are transported using the *Lin and Rood* [1996] advection scheme. The integrations described in this paper use output from MACCM2. The reasons for this choice are described in [*Douglass et al.,* 1999].

The horizontal resolution of the MACCM2 is 5.6° longitude by 2.8° latitude. The output fields were interpolated to the standard 5° by 4° grid of the GMI model. The GMI model adopts the 44 vertical levels of the MACCM2. The vertical resolution is $\sim$ 1 km at the tropopause, degrading to a minimum vertical resolution of $\sim$2.5 km.

The Southern Hemisphere temperatures from the standard MACCM2 simulation are 30°-40° too cold, and the polar night jet is $\sim$ 50 m s^{-1} too strong compared to observations. Following *Brasseur et al.* [1997], the GMI model utilizes a data set from a modified version of the MACCM2 (MACCM2′), which results in a more realistic simulation of the Southern Hemisphere high-latitude lower stratosphere. In the MACCM2′ gravity wave parameterization, a source of gravity waves with non-zero phase speeds was added to the standard orographically forced zero phase speed gravity wave source to account for forcing of gravity waves by shear instabilities, frontal propagation, and convection. The result of this additional forcing is a significantly improved Southern Hemisphere simulation. However, the occurrence of cold temperatures during the Northern Hemisphere winter is much less frequent than is observed. Consequently, the Northern Hemisphere winter simulation will not be considered in this paper.

The GMI model does not predict the concentrations of H_2O in the atmosphere, because of the difficulty of

representing tropospheric hydrological processes. Instead, it uses zonal mean H_2O fields which change monthly. There are two sources for these distributions depending on whether the simulation is for the present-day or future atmosphere.

For present-day atmosphere simulations, the H_2O fields are derived from monthly zonal means of microwave limb sounder (MLS) observations [*Lahoz et al.*, 1996]. In regions where no MLS data are available (above and below the MLS measurement range and outside of the latitudes observed by the MLS instrument), the GMI H_2O distributions are from the output of a "constrained" version of the the GSFC 2-D model [*Jackman et al.*, 1996]. The H_2O fields in this version of the GSFC model are set to the MLS monthly zonal mean values where those data exist but are predicted by the model chemistry and dynamics outside of those regions. The MLS data act as a boundary condition for the portions of the GSFC model domain outside of the MLS measurement region, and the results are global H_2O distributions consistent with the measurements but predicted by the model chemistry and dynamics. For simulations of the future atmosphere the GMI H_2O distributions are taken from a free-running version of the GSFC 2-D model using surface source gas boundary conditions appropriate for the simulated year.

To predict ice surface area densities (SADs), PSC-induced dehydration, and HSCT response, the GMI model must use a background H_2O distribution that does not itself show the effects of atmospheric dehydration processes. The GSFC 2-D model simulations of future atmosphere H_2O concentrations were therefore made without the model PSC parameterization. We replaced the dehydrated regions of the high-latitude Southern Hemisphere lower stratosphere in the MLS H_2O distributions with an estimate of the H_2O mixing ratios that would occur at these locations in the absence of PSC-induced dehydration. We estimated H_2O in the absence of PSC-induced dehydration by regressing Cryogenic Limb Array Etalon Spectrometer (CLAES) N_2O retrievals [*Roche et al.*, 1996] and MLS H_2O at lower latitudes (-30° - 30°) and pressures between 46.4 and 2.2 hPa. Low H_2O values at high latitudes were then replaced with estimates using the H_2O-N_2O relationship. While the approximate conservation of $2CH_4 + H_2$ in the stratosphere suggests CH_4 as the logical choice for this procedure, we are more familiar with CLAES N_2O. N_2O is a long-lived tracer possessing a compact and approximately linear relationship to CH_4, so its use here is justified.

A zonally symmetric background sulfate aerosol SAD distribution is also incorporated into the model. This distribution was constructed from surface area density estimates obtained from Stratospheric Aerosol and Gas Experiment (SAGE) II observations of aerosol extinction in 1995 [*Thomason et al.*, 1997].

3. PSC Parameterization

The GMI PSC parameterization is designed to provide a realistic representation of the formation, growth, evaporation, and sedimentation of PSCs which will respond to aircraft emissions, only without an explicit treatment of particle microphysics. We describe the parameterization in detail here as some of its features differ from current 3-D model PSC treatments as exemplified by *Chipperfield et al.*, [1993].

The parameterization calculates SADs for both Type 1 and Type 2 PSCs. The Type 1 PSC composition can be set to either nitric acid trihydrate (NAT) or supercooled ternary sulfate (STS). Numerous recent studies have indicated that Type 1 PSCs are frequently STS, so we assume an STS composition in this study [e.g., *Dessler et al.*, 1999; *Carslaw et al.*, 1994; *Drdla et al.*, 1994; *Del Negro et al.*, 1997; *Massie et al.*, 1997; *Santee et al.*, 1998]. Type 2 PSCs are modeled as water ice with a coexisting NAT phase as described in more detail below.

Equilibrium vapor pressure relationships and user-specified supersaturation ratios determine the temperatures at which HNO_3 and H_2O will condense out of gas phase into PSCs. Since the gas and condensed phase HNO_3 and H_2O concentrations equilibrate immediately, this may be referred to as a thermodynamically based (rather than microphysical) calculation.

The parameterization assumes that the mass condensed into PSCs is distributed in particles obeying log-normal size distributions,

$$\mathcal{N}(r) = \frac{N}{\sqrt{2\pi} r \ln(\sigma)} \exp\left(\frac{-\ln^2\left(\frac{r}{r_o}\right)}{2\ln^2(\sigma)}\right), \qquad (1)$$

where N is the number of aerosol particles per cubic centimeter, r is the particle radius, r_o is the median particle radius, and $\ln(\sigma)$ is the standard deviation of the normal distribution obeyed by the logarithm of the particle radius, $\ln(r)$. The user specifies N and σ for each aerosol type. In this case the median radius r_o becomes a variable determined by the condensed phase mass in a particular grid box. Alternatively, the user can specify σ and r_o, which results in a variable particle number density N. Here N and σ are specified for each aerosol type. Changes in condensed phase mass due to condensation and evaporation produce variations in particle size rather than number, which is more physically realistic.

The rate at which condensed HNO_3 and H_2O in a model grid box sediments to lower altitudes is derived from the aerosol size distribution as described in section 3.3. If the temperatures at these altitudes are above PSC condensation temperatures, the condensed phase mass is returned to the gas phase. The condensed phase constituents are also subject to transport by the model wind fields, so particle fall velocities are relative to the air mass in which the aerosol particles are located.

3.1. Type 2 PSCs

The equilibrium vapor pressure of H_2O over H_2O ice is calculated using the work of *Marti and Mauersberger* [1993]. Type 2 PSCs form when the ratio between the ambient H_2O vapor pressure and the equilibrium vapor pressure exceeds a supersaturation ratio, which is currently set to 1.4. This corresponds approximately to a 2° supercooling, consistent with the estimates of *Tabazadeh et al.* [1997].

In this study the ice aerosol size distribution is specified with $N = 0.01$ ice particles cm^{-3} and $\sigma = 1.6$. These values are consistent with Forward Scattering Spectrometer Probe (FSSP) size distribution measurements made in Type 2 PSCs by the NASA ER-2 aircraft during the Airborne, Arctic Stratospheric Experiment (AASE) mission in January 1989 [*Dye et al.,* 1992]. Type 2 PSCs are apparently the only particles in the stratosphere which grow large enough to carry significant amounts of HNO_3 or H_2O out of the stratosphere through sedimentation. Thus the observed widespread denitrification of the Antarctic polar vortex [*Rinsland et al.,* 1996; *Santee et al.,* 1998; *Fahey et al.,* 1989] suggests that large amounts of HNO_3 are being transported out of the stratosphere by Type 2 PSCs. The mechanism by which this is accomplished is currently not understood [*Peter*, 1997].

Leu [1988] and *Hanson* [1992] both measured rapid uptake of HNO_3 on laboratory ice surfaces, consistent with a mass accommodation (sticking) coefficient of 0.3. Hanson also noted that the vapor pressures over the HNO_3 layer were initially too high to be consistent with a NAT composition, but on timescales of several hours the vapor pressures over HNO_3/H_2O coatings on ice were consistent with NAT. We therefore assume that a NAT phase cocondenses with the ice particles when Type 2 PSCs form, so HNO_3 is removed from the gas phase in accord with the measured equilibrium vapor pressure of HNO_3 over NAT as given by *Hanson and Mauersberger* [1988]. Note, however, that the evaporation of a Type 2 PSC does not leave a Type 1 PSC composed of NAT if an STS composition has been assumed for the Type 1 PSCs. Instead, the released HNO_3 becomes incorporated into Type 1 PSCs with an STS composition.

3.2. Type 1 PSCs

When a NAT composition is chosen for Type 1 PSCs, saturation and nucleation temperatures for NAT are determined from the work of *Hanson and Mauersberger* [1988] using ambient H_2O and HNO_3 concentrations, the local temperature, and a user-specified threshold supersaturation ratio. The default supersaturation ratio is 10, which corresponds to a supercooling of $\sim 3^o$ and is consistent with the calculations of *Peter et al.* [1991]. Vapor phase H_2O concentrations are assumed to be unaffected by NAT condensation, because the concentration of H_2O typically exceeds that of HNO_3 by 2 - 3 orders of magnitude.

When an STS composition is assumed for the Type 1 PSCs (as was the case in this study), the condensed phase mass is calculated following *Carslaw et al.* [1995]. The lognormal size distribution for STS is specified by $N = 10$ particles cm^{-3} and $\sigma = 1.6$. Since N is consistent with the observed total number density of stratospheric particles [e.g., *Dye et al.,* 1992], the code effectively assumes that all background liquid binary sulfate (LBS) aerosol particles swell in response to the uptake of HNO_3 and H_2O at cold polar temperatures.

The ambient H_2SO_4 concentration is inferred from the background sulfate aerosol distribution, which allows feedback between the PSCs and the sulfate aerosols. At cold temperatures the volume density of STS aerosol is more sensitive to HNO_3 and H_2O concentrations than it is to H_2SO_4, so this approach should be adequate. Also, the inferred H_2SO_4 mixing ratios are in good agreement with estimates from model calculations which explicitly treat the sulfur cycle (D. Weisenstein, personal communication, 1997).

3.3. Sedimentation

The GMI PSC parameterization accounts for sedimentation of HNO_3 and H_2O condensed into both Type 1 and Type 2 aerosols. The calculation of the constituent sedimentation flux is consistent with the size distribution assumptions discussed in sections 3.1 and 3.2. This flux can differ substantially with that calculated for a monodisperse size distribution. Assuming a Stokes' law relationship between particle size and fall velocity (i.e., the fall velocity is proportional to the square of the particle radius), we calculate that the flux of a lognormally distributed sedimenting particle population is given by $J = nv_o \exp(8 \ln^2 \sigma)$, where J is in units of molecules per unit area per second, n is the number density of condensed phase molecules of sedimenting constituent in molecules per unit volume, v_o is the fall velocity of a particle with a radius equal to the median radius r_o of the size distribution, and $\ln(\sigma)$ is defined as in equation (1). This exceeds the flux from a monodisperse distribution with the same N and condensed phase volume density V (and hence a larger radius) by a factor of $\alpha = \exp(5 \ln^2 \sigma)$. For $\sigma = 1.6$, $\alpha \simeq 3$. We use fall velocities calculated by *Kasten* [1968] to determine v_o from r_o and then adjust to obtain the proper mass flux.

It should be noted that J is sensitive to σ. Increasing σ by 20% increases J by a factor of 2.8, and decreasing σ by 20% decreases J by a factor of 0.45. Since $\pm$ 20% variations are within observational constraints, we discuss the sensitivity of our results to a change in σ in sections 6 and 7.

Sedimentation of condensed phase HNO_3 is straightforward because HNO_3 is a transported species in the model. The condensed phase fraction of the ambient HNO_3 distribution calculated by the PSC parameterization is simply subjected to an additional vertical transport step with velocity αv_o. H_2O sedimentation is more

difficult because the GMI code uses a specified rather than calculated background H_2O distribution. Thus it is necessary to keep track of the amount of H_2O which has condensed and sedimented to other model levels. We do this by introducing an additional transported species named "dehyd." Dehyd is produced when the condensed phase H_2O at a particular grid box sediments to lower levels, and it is lost when condensed phase H_2O sediments into the grid box from above. The ambient H_2O concentration (gas plus condensed phase H_2O) at any location is then calculated as the difference between the background H_2O distribution and dehyd. Note that dehyd can be negative; this corresponds to a moistening of a layer above the background amount of H_2O as a result of particle sedimentation from above.

4. Data Sources

In this paper we compare model output from the base simulation described in section 5 to CLAES retrievals of HNO_3. We use version 7 data because the version 8 retrieval algorithm appears to be high biased in the Southern Hemisphere high-latitude winter and the CLAES investigators recommend version 7 over version 8 in this case (J. Kumer, private communication, 1999). Estimated systematic errors in the version 7 retrieval range from 14 to 12% in the lower stratosphere between 70 and 30 hPa, while random errors are estimated to be between 12 and 7% over the same pressure levels. Included in the systematic error estimate is a low bias in the CLAES temperature retrieval [*Gille et al.,* 1996] which is thought to produce ~9% overestimates of HNO_3 at a temperature of $\sim$ 190 K [*Kumer et al.,* 1996].

We also compare model output with measurements of H_2O made by MLS. We use version 3 retrievals [*Lahoz et al.,* 1996] although version 4 data is currently available. The version 3 data are more appropriate for comparison to the model, because version 3 MLS data were used to construct background H_2O distributions for the model as described in section 2.

An Atmospheric Laboratory for Applications and Science (ATLAS) payload was flown on board the space shuttle in November 1994 [*Kaye and Miller,* 1996]. This payload carried the Atmospheric Trace Molecule Spectroscopy (ATMOS) instrument, a Fourier transform spectrometer [*Gunson et al.,* 1996]. ATMOS measured N_2O, H_2O, and the primary constituents of NO_y in addition to other species at latitudes between 64.5°S and 72.4°S in the Southern Hemisphere during sunrise solar occultations between November 3 and 14, 1994. The Southern Hemisphere polar vortex was intact and stable during this period, resulting in numerous profiles taken both inside and outside of the vortex [*Manney et al.,* 1996]. Lower stratospheric 1σ precision errors in H_2O and N_2O are estimated to be less than 5%. *Rinsland et al.* [1996] estimate the error in NO_y constructed from the ATMOS observations to be $\sim$ 15%. These observations are used to quantify vortex dehydration and denitrification and are discussed and compared to the GMI model in section 6.

5. Model Simulation

This paper discusses the results of three different runs of the GMI CTM, which will be referred to as the "base," "subsonics-only," and "HSCT-perturbed" runs. The base run was designed to allow comparisons with observations and approximates atmospheric conditions in 1995 - 1996. No aircraft emissions were included in this run. The subsonics-only and HSCT-perturbed runs are scenarios 1 and 4, respectively, as specified in Table 4-3 of the most recent NASA aircraft assessment document [*Kawa et al.,* 1999]. The subsonics-only run was designed to approximate atmospheric conditions anticipated for the year 2015, including emissions of NO_x and H_2O representing an aircraft fleet which does not include HSCTs. The HSCT-perturbed run replaces a portion of the 2015 subsonic fleet with emissions from a fleet of 500 HSCTs flying at $\sim$ 18 km and emitting 5 g of NO_x per kilogram of fuel burned. Note that this scenario does not include potential HSCT emission of H_2SO_4. The neglect of aircraft H_2SO_4 is discussed in section 7.

The base simulation was integrated for 5 model years. The subsonics-only and HSCT-perturbed simulations were run for 6 years. This is long enough to achieve an approximately repeating annual cycle negligibly affected by the model initial condition. The chemical mechanism for all three runs was basically the same as that used in the NASA AEAP chemistry benchmark intercomparison [*Stolarski et al.,* 1995], modified to include source gas reactions. It is a fairly complete representation of stratospheric chemistry including 46 species. Of these, 43 were transported, while H, $O(^1D)$, and N were inferred assuming photochemical equilibrium. The mechanism considered catalytic destruction of O_3 by radicals in the O_x, HO_x, NO_x, Cl_x, and Br_x families. Reaction rates and photolysis cross sections were taken from *DeMore et al.* [1997]. The six standard heterogeneous reactions listed in that publication were included on the background sulfate aerosol and PSCs using the specified sticking coefficients.

One difference in the chemical mechanism between the base simulation and the aircraft runs was the inclusion in the base run of a channel for the reaction of ClO and OH to produce HCl. *Lipson et al.* [1997] measured a 0.06 ± 0.02 branching ratio for this channel, and *Lary et al.* [1995] showed that this channel could somewhat enhance the rate of Cl_x deactivation at the poles during spring. The *Lipson et al.* study was published too late for the reaction to be included in the *DeMore et al.* [1997] reaction rate compilation. It was therefore not included in the aircraft runs in keeping with current aircraft assessment conventions. Its neglect should not change any of the basic conclusions of this paper.

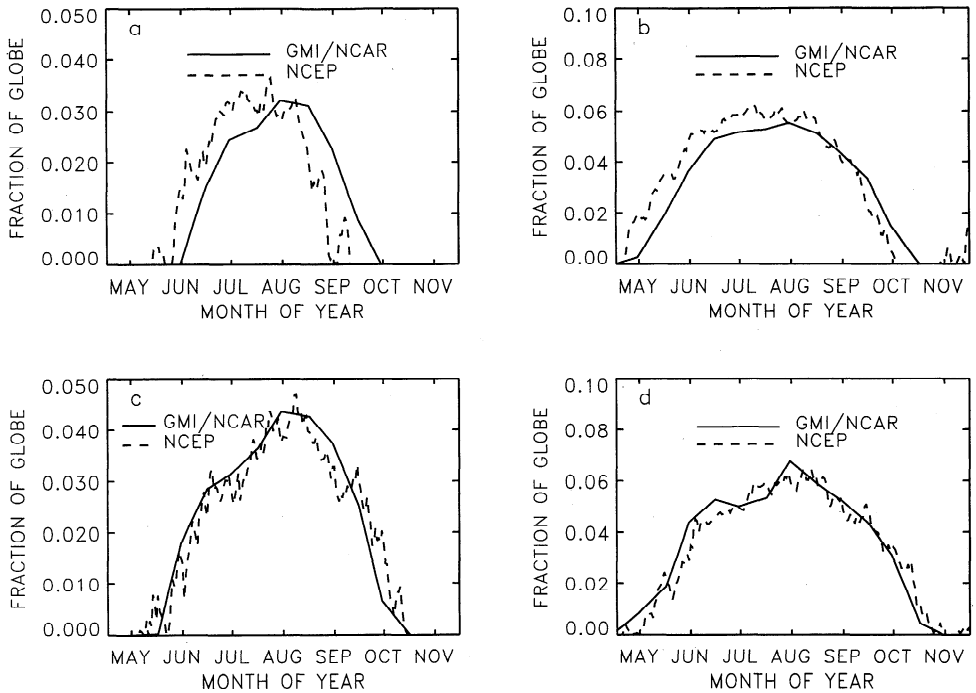

Figure 1. Fraction of global surface area below 190 and 200 K between May and November in the Global Modeling Initiative (GMI) Chemistry and Transport Model (CTM) compared with results using National Center for Environmental Prediction (NCEP) temperature distributions in 1992. The solid line represents the GMI model using National Center for Atmospheric Research (NCAR) Middle Atmosphere Community Climate Model version 2′ (MACCM2′) temperatures. The dashed line represents the global area fraction calculated using NCEP temperatures. (a) Fraction below 190 K at 47 hPa (model) and 50 hPa (NCEP). (b) Fraction below 200 K at 47 hPa (model) and 50 hPa (NCEP). (c) Fraction below 195 K at 105 hPa (model) and 100 hPa (NCEP). (d) Fraction below 200 K at 105 hPa (model) and 100 hPa (NCEP).

6. Results

6.1. Polar Temperatures

The behavior of the PSC parameterization depends sensitively on the temperature distribution, so we first compare the MACCM2′ temperatures used in the model simulation with observations from 1992.

Figure 1 compares the MACCM2′ areal fraction of the globe below 190 and 200 K on the 50 hPa surface (Figures 1a and 1b) and the areal fraction of the globe below 195 and 200 K on the 100 hPa pressure surface (Figures 1c and 1d) with National Center for Environmental Prediction (NCEP) temperatures during 1992. The solid line represents the MACCM2′ global area fractions, and the dashed line shows the corresponding quantity calculated using NCEP temperature distributions. Cold regions in the tropics (30°S - 30°N) do not contribute to the global area fractions in Figure 1.

Figure 1a shows that in both the model and the atmosphere, global area fractions below 190 K reach ~ 0.03, but the model peaks ~ 20 days later than the atmosphere does in 1992. Figure 1a also shows that the atmosphere gets cold earlier than in the model, with the model lagging the atmosphere by between 10 and 20 days in June and July. Figure 1a indicates that the atmosphere warms up before the model does, so the model global area fraction below 190 K is larger than that seen in the atmosphere during the Southern Hemisphere spring of 1992.

In Figure 1b, peak MACCM2′ global area fractions below 200 K lag the atmosphere by ~ 20 days. Peak values are also ~ 20% lower than the observations. (The MACCM2′ temperature distributions underestimate peak global area fractions below 200 K in all years between 1990 and 1997, with the discrepancy in 1992 being typical.) During September the agreement between model and observations is good, while during the October time frame the model global area fraction below 200 K is somewhat higher than the observations.

Figures 1c and 1d show that at 100 hPa the MACCM2′ global area fractions below 195 and 200 K are very similar to atmospheric values in 1992. Overall, Figure 1 suggests that model temperature distributions in the Southern Hemisphere late fall, winter, and early spring agree well enough with observed temperatures to make qualitative comparisons of modeled and observed quantities, provided the differences between the two are kept in mind.

6.2. Polar Stratospheric Clouds

Few observations of PSC SADs exist, precluding a robust evaluation of the model predictions throughout the Southern Hemisphere winter and spring. However, model-predicted surface area densities and size distribution median radii are consistent with available observations. Typical ice aerosol median radii at the 50 hPa level are $\sim$ 5 μm and STS aerosol radii are consistently $\sim$ 0.2 - 0.3 μm. These values roughly agree with aerosol particle sizes inferred from observations [*Dye et al.*, 1992; *Beyerle et al.*, 1997]. In August at $\sim$ 50 hPa, STS SADs range up to 15 $\mu m^2 cm^{-3}$, and ice SADs are $\sim$8 $\mu m^2 cm^{-3}$. These values are consistent with the observations of *Dye et al.* [1992] and *Gobbi et al.* [1998].

Figures 2a and 2b show the time evolution of vortex-averaged ice and STS SADs, respectively, in the Southern Hemisphere between May and November. (Figures 2-15 were constructed from semimonthly model output occurring on the fifteenth and final day of each month.) In this paper we define the vortex edge using Ertel's potential vorticity gradient as in the work of *Nash et al.* [1996]. Note that the STS SAD plotted in Figure 2b does not include the background sulfate aerosol SAD. It is instead the increase in SAD that has resulted from HNO_3 and H_2O uptake and subsequent swelling of the aerosol particles. Vortex-averaged background sulfate aerosol SADs range from $\sim$ 1 $\mu m^2 cm^{-3}$ at 100 hPa to values less than 0.1 $\mu m^2 cm^{-3}$ above 10 hPa. (The STS SAD distribution plotted in Figure 2b and the background sulfate aerosol SAD distribution are combined when heterogeneous reactions rates are calculated.)

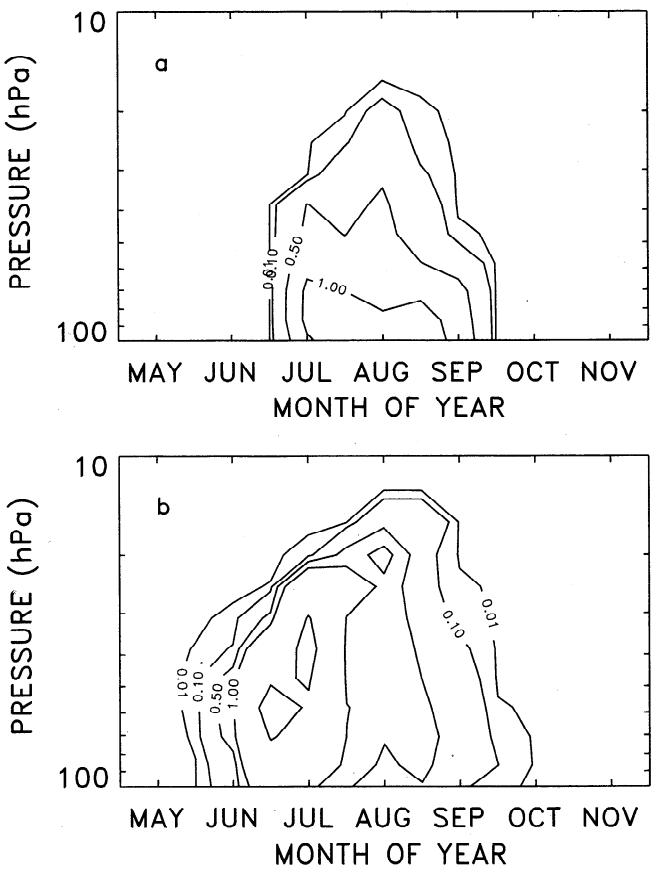

Figure 2. Southern Hemisphere vortex averaged polar stratospheric cloud (PSC) surface area densities (SADs), in $\mu m^2 cm^{-3}$, from May through November in the altitude range between 100 and 10 hPa. (a) Type 2 (ice) SAD. (b) Type 1 (supercooled ternary sulfate (STS)) SAD.

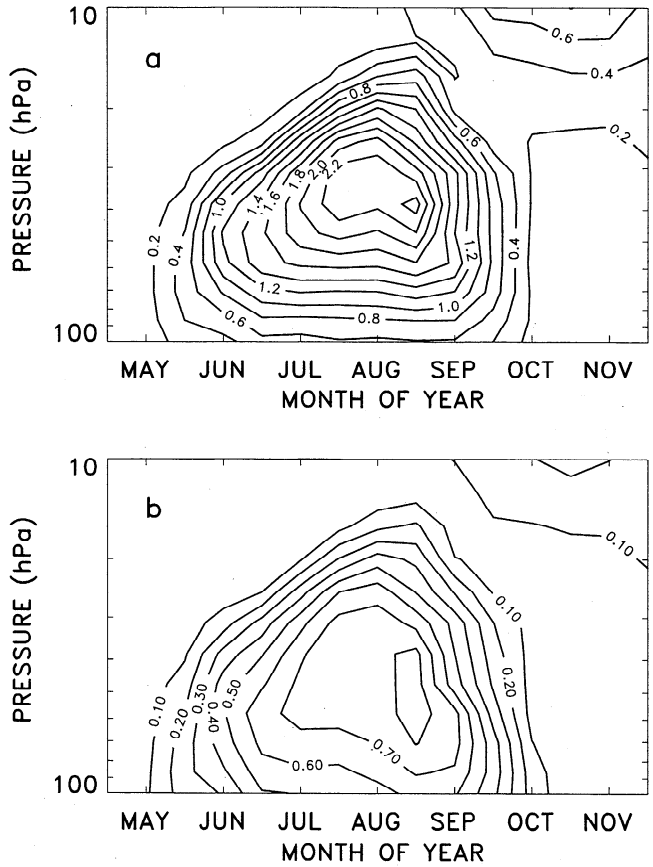

Figure 3. Southern Hemisphere vortex-averaged active Cl_y, in (a) parts per billion by volume and (b) fraction of total Cl_y. Active Cl_y is defined as all forms of inorganic chlorine except the reservoir species HCl and $ClONO_2$.

Figure 2a indicates that ice aerosol SADs exceed .01 $\mu m^2 cm^{-3}$ in July, August, and September. Peak vortex-averaged values of just over 1.2 $\mu m^2 cm^{-3}$ occur in late July between 80 and 100 hPa. Significant ice SADs extend as high as 20 hPa. Figure 2b shows that STS SADs are significant from June through September. Peak values of $\sim$ 5 $\mu m^2 cm^{-3}$ occur in late June and early July between 30 and 70 hPa.

The STS and ice SADs shown in Figure 2 are sufficient to activate inorganic chlorine, as shown in Figures 3a and 3b. Figure 3a shows the vortex-averaged amount of active Cl_y in parts per billion by volume (ppbv), where active Cl_y is defined as all inorganic chlorine other than HCl or $ClONO_2$. Peak active Cl_y values

of ~ 2.4 ppbv occur at the end of August between 30 and 50 hPa. Figure 3b indicates that this is ~ 80% of all the inorganic chlorine in the model at this level, so Cl_y peaks at ~ 3 ppbv. At 60 hPa, the approximate flight altitude of the ER-2 research aircraft, total Cl_y in the GMI model is ~ 2 ppbv. This value is ~ 30% lower than estimates of Cl_y made from Airborne Antarctic Ozone Expedition (AAOE) N_2O observations using the Woodbridge relationship [*Considine,* 1999; *Woodbridge et al.,* 1995]. The halogen activation resulting from heterogeneous reactions on PSCs creates a well-developed and timed O_3 hole, with minimum column O_3 values reaching ~ 120 Dobson units (DU) in October, similar to observations. This is illustrated in Figure 4, which compares Earth Probe Total Ozone Mapping Spectrometer (EP TOMS) monthly zonal mean column O_3 in 1997 as a function of month of year and latitude with the GMI model calculation. We use 1997 EP TOMS data because it is the complete year of TOMS data which is chronologically closest to the model simulation conditions. Since the comparison is qualitative, the year compared is not critical. While available observations of PSC SADs are not sufficient to directly test PSC occurrence in the GMI model, the PSCs that do form produce O_3 concentrations in reasonable agreement with observations.

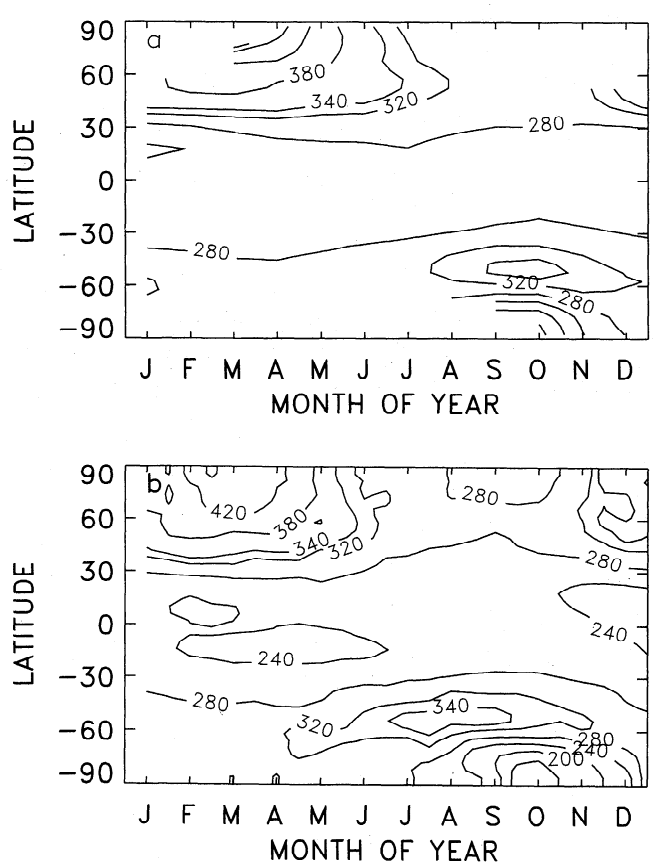

Figure 4. Column O_3 from observations and the GMI model. (a) Column O_3 values retrieved by Earth Probe Mapping Spectrometer (EP TOMS) in 1997. Figure 4a was constructed from monthly zonal means for 1997. (b) Column ozone in the GMI model. The model used MACCM2′ winds and temperatures, and 1995 source gas boundary conditions.

In section 3.3 we noted that the sedimentation mass flux was sensitive to the width of the size distributions assumed for the PSCs. It is possible that the PSC SADS are sensitive to σ as well. We therefore made another model run with the σ for both Type 1 and Type 2 PSCs reduced by 20% (to $\sigma = 1.3$), a change which reduces the sedimentation mass flux by ~ 55%. The reduced σ results in substantial increases in PSC SADs. For instance, at 47 hPa the largest difference in the vortex-averaged STS SAD between the $\sigma = 1.3$ and $\sigma = 1.6$ cases is ~ 75%, occurring in mid-August. The largest difference in the vortex-averaged ice SAD between these two cases is ~ 160% at the end of August.

Although there is a substantial difference in PSC SADs in these two cases, the additional SAD does not activate any more Cl_y. Hence O_3 concentrations are not significantly different.

6.3. Denitrification

When temperatures drop to the values required for PSC formation in the GMI model, HNO_3 and H_2O condense out of gas phase into PSC particles, which are subject to sedimentation. The condensation depletes the gas phase concentrations of these constituents, while sedimentation moves the condensed molecules to lower levels and can make the removal of gas phase HNO_3 and H_2O permanent.

Figure 5 shows the evolution of gas phase HNO_3 from mid-June through mid-September in the GMI model at high latitudes on the 47 hPa surface. On June 15, HNO_3 mixing ratios are typically above 7 ppbv, but there is a small region near the pole where HNO_3 condensation into STS aerosols is beginning. HNO_3 mixing ratios are as low as 5 ppbv, while the temperatures in this region are just above the frost point.

A month later an extensive region of very low HNO_3 has formed, with HNO_3 concentrations dropping below 1 ppbv. Relatively high HNO_3 mixing ratios encircle the low HNO_3 region, with magnitudes about the same as those on June 15. On August 15 the low HNO_3 region is slightly larger than in mid-July. The lowest mixing ratios occur in the regions where the temperature falls below the frost point. Also, mixing ratios in the high HNO_3 ring surrounding the low HNO_3 region have decreased by over 40% from the previous month. By mid-September the area enclosed by the 1 ppbv contour has decreased, indicating that recovery of the low HNO_3 region has begun. At the same time, mixing ratios in the high HNO_3 ring have decreased further.

Figure 6 shows gas phase HNO_3 at 46.4 hPa observed by CLAES on June 15, July 10, August 17, and September 15, 1992, at high Southern latitudes. Note that the grey scale for Figure 6 differs from that of Figure 5.

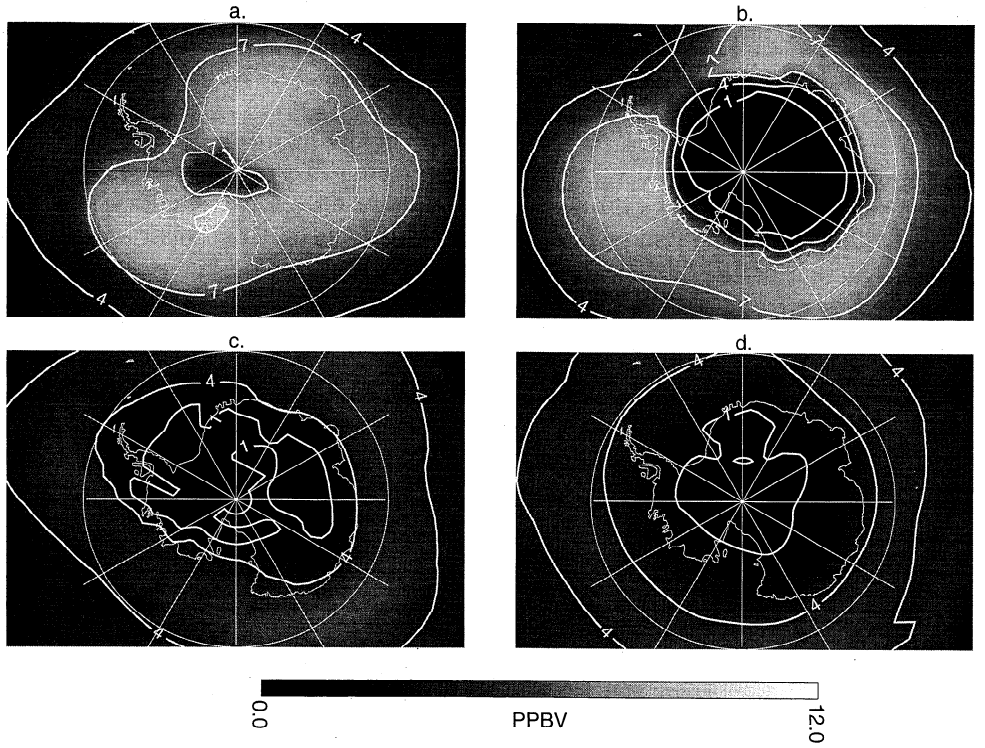

Figure 5. HNO_3 predicted by the GMI 3-D CTM at 47 hPa on (a) June 15, (b) July 15, (c) August 15, and (d) September 15.

On June 15 a low HNO_3 region is observed by CLAES that is significantly larger than that occurring in the GMI model. This is consistent with the 2 - 3 week time lag in the occurrence of cold model temperatures compared to 1992 observations as shown in Figure 1. HNO_3 mixing ratios ringing the low HNO_3 region are higher than those in the GMI model run, exceeding 13 ppbv at some locations. By July 10 the low mixing ratio region

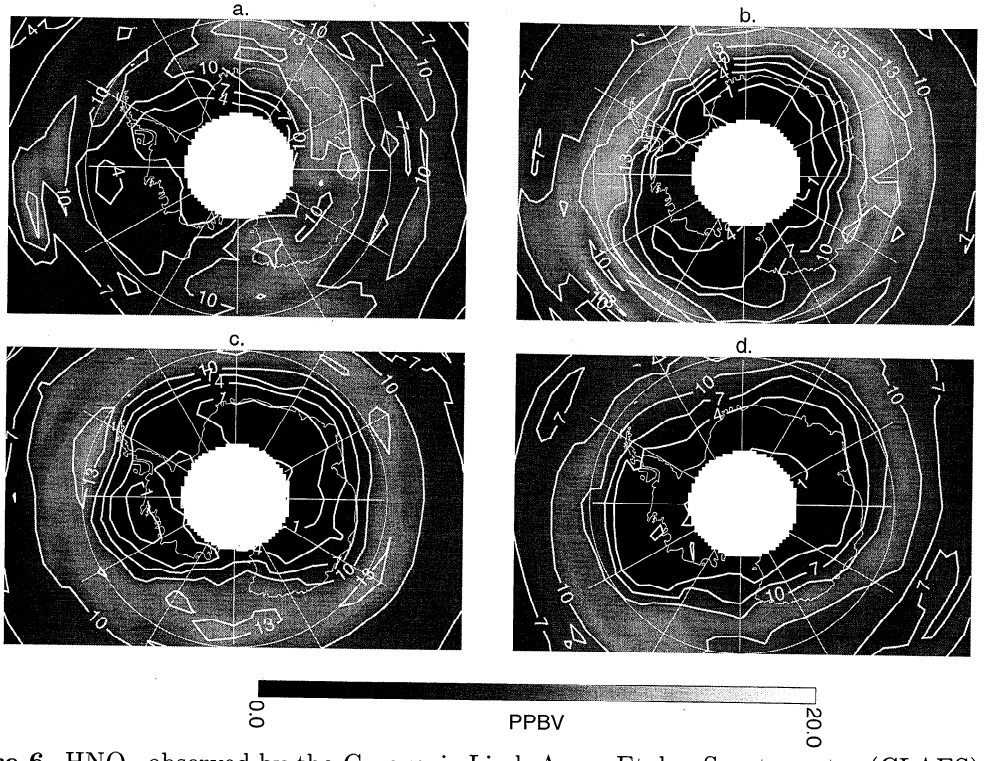

Figure 6. HNO_3 observed by the Cryogenic Limb Array Etalon Spectrometer (CLAES) instrument on the 46.4 hPa surface on (a) June 15, (b) July 10, (c) August 17, and (d) September 15.

has expanded and deepened, with values below 1 ppbv occurring. Values in the high mixing ratio ring are similar to those seen in mid-June. The low HNO_3 region reaches its greatest extent in mid-August, while mixing ratios in the high HNO_3 ring remain steady. In mid-September the area enclosed by the 1 ppbv contour has diminished substantially. In addition, peak HNO_3 concentrations in the ring region have decreased relative to the mid-August values. Note that the behavior of gas phase HNO_3 at 46.4 hPa observed by MLS is similar to the CLAES HNO_3 distributions (see the work of *Santee et al.* [1998] for a more complete discussion of the similarities and differences).

Comparison of Figures 5 and 6 shows that the temporal evolution of HNO_3 concentrations in the lower stratosphere in the GMI model qualitatively agrees with the observations. However, the most obvious difference between Figures 5 and 6 is the much lower mixing ratios in the GMI model compared to the observations. Two factors unrelated to PSC sedimentation contribute to these low values. First, the overall amount of NO_y in the model is low. This can be seen by comparing model and observed midlatitude NO_y-N_2O correlation plots [*Kawa et al.*, 1999]. Second, the model places the peak of the vertical profile of high-latitude HNO_3 substantially above its observed location, possibly because of weak descent in the polar vortex during polar winter. Both these factors result in lower HNO_3 mixing ratios in the lower stratosphere and complicate the evaluation of the model sedimentation.

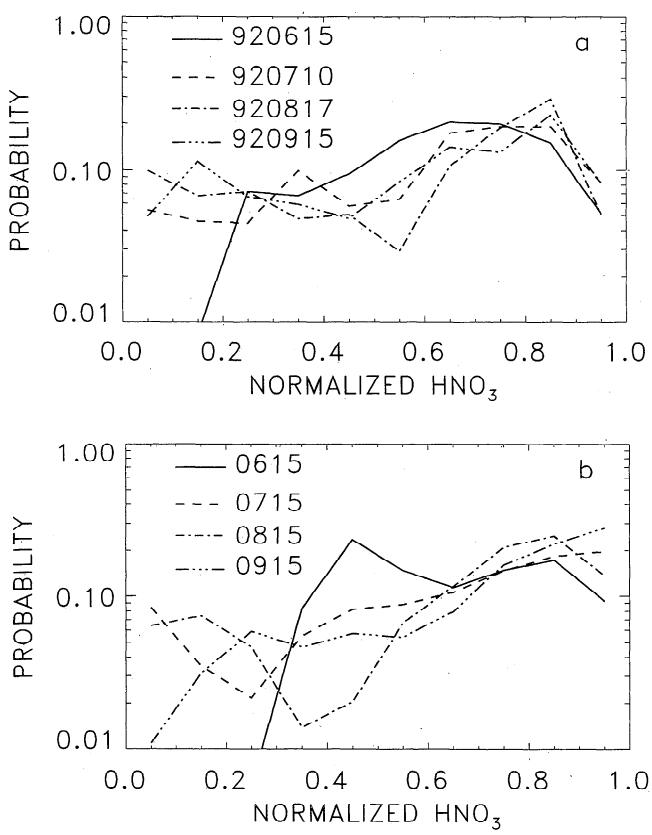

Figure 7. Normalized HNO_3 probability distributions constructed from (a) 46.4 hPa CLAES HNO_3 observations and (b) 47 hPa values calculated by the GMI model. The distributions were constructed from the normalized HNO_3 maps shown in Figures 6 and 7.

Although Figure 1 shows that the evolution of low-temperature regions is similar in the lower stratosphere in the model and the 1992 atmosphere, the differing model and atmospheric meteorologies complicate map-based comparisons. An alternative is to compare probability distributions of the occurrence of HNO_3 concentrations. Figure 7a shows four probability distributions constructed from CLAES HNO_3 retrievals at 46.4 hPa. To facilitate comparison with the GMI model results, the HNO_3 mixing ratios have been normalized by taking its ratio to the maximum observed value on the 46.4 hPa surface south of -50°, so the HNO_3 values range between 0 and 1. Figure 7a shows the area-weighted probability of occurrence of normalized HNO_3 between -80° and -50° on June 15, July 10, August 17, and September 15, 1992. Figure 7b shows the corresponding plot from the GMI model output. Note that the ordinate is plotted on a logarithmic scale to emphasize the lower occurrence probabilities.

Overall, the GMI and CLAES probability distributions are similar. In both the model and the observations there is a general increase in the probability of occurrence for larger normalized HNO_3 values, and the occurrence probabilities are similar. The later onset of denitrification in the GMI model evident in the comparison of Figures 5 and 6 is seen in the June 15 model probability distribution with smaller than observed occurrence probabilities for normalized $HNO_3 < 0.3$ and larger occurrence probabilities for normalized HNO_3 values between 0.3 and 0.5. Figure 7b also shows lower than observed occurrence probabilities in July for normalized HNO_3 between 0.1 and 0.4 and in August between 0.3 and 0.5, indicating steeper spatial gradients in the model between the high and low values of HNO_3 than in the CLAES observations. At the lowest values, less than 0.2 of the maximum value, the model and the observations both have the largest occurrence probabilities in mid-August. In September, however, the model significantly underestimates the occurrence probabilities at low normalized HNO_3 concentrations.

The high-latitude evolution of HNO_3 concentrations over the course of the winter is governed by both dynamics and PSC sedimentation. The comparisons made above do not therefore allow a direct comparison of the effects of PSCs. One way of isolating the effects of PSCs is by exploiting the strong correlation that exists between NO_y and N_2O in the lower stratosphere in the absence of rapid loss of NO_y due to PSCs. *Fahey et al.* [1989] showed that a quantity NO_y^* can be defined from the correlation to predict from the N_2O concentration in a region influenced by PSC processes the NO_y that would exist there in the absence of PSC-induced condensation and sedimentation. The differ-

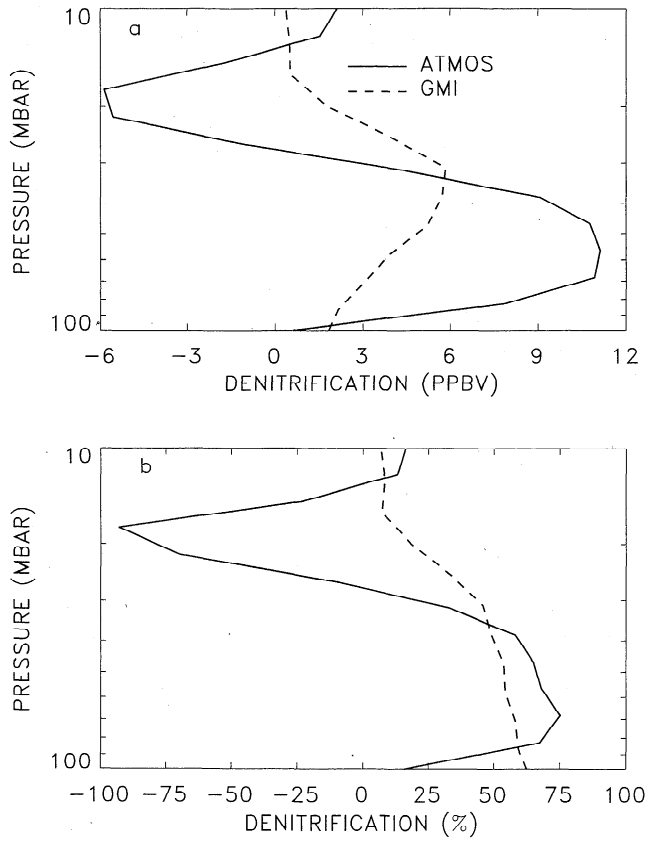

Figure 8. Vortex average ΔNO_y ($= NO_y^* - NO_y$) in (a) parts per billion by volume (ppbv) and (b) percentage, constructed from Atmospheric Trace Molecule Spectroscopy (ATMOS) observations (solid line) and GMI model output (dashed line) as described in the text.

ence $\Delta NO_y = NO_y^* - NO_y$ is then a measure of the change in NO_y due only to condensation and sedimentation processes.

Rinsland et al. [1996] used the ATMOS observations discussed in section 4 to construct NO_y^* and obtain an observation of extensive denitrification in the lower stratosphere polar vortex during November 1994. Figure 8 compares profiles of vortex-averaged ΔNO_y constructed from the ATMOS observations using the method of Rinsland et al. (solid lines) and GMI model output (dashed lines). NO_y^* for the GMI model was calculated by using N_2O and NO_y mixing ratios at model locations outside of but within 10° in latitude of the polar vortex edge to define a fit between NO_y and N_2O. From this fit, NO_y^* was calculated throughout the polar vortex. Figure 8a compares ΔNO_y in mixing ratio units, and Figure 8b compares ΔNO_y expressed as a percent denitrification. Figure 8a shows large-scale denitrification of the polar vortex in November 1994, with peak values reaching 11 ppbv between 50 and 60 hPa. The peak denitrification in the GMI model is $\sim$ 50% as large as that observed and occurs at 30 hPa, $\sim$ 3.5 km higher than the ATMOS result. Note that the large negative values seen in the ATMOS observations at 20 hPa have been attributed by Rinsland et al. to descent of mesospheric air with a different NO_y/N_2O relationship. This is not reproduced in the GMI model.

Although the absolute values of lower stratospheric denitrification in the GMI model do not compare well with observations, in relative terms the agreement is good. Figure 8b shows that lower stratospheric model denitrifications of 50 - 60% occur in the model lower stratospheric polar vortex, compared to observed denitrification of up to 75%. The good agreement of relative denitrification between the model and the observations suggests that the differences seen in Figure 8a do not indicate a problem with the PSC parameterization but are more likely due to the overall underestimation of NO_y in the model and weak descent in the model polar vortex.

The results presented here do not change much when σ is reduced by 20%. There are small differences in the evolution of HNO_3 concentrations through the winter and the residual denitrification of the springtime lower stratospheric Southern Hemisphere vortex. For instance, the lower stratospheric model denitrifications of 50 - 60% seen in Figure 8b are reduced to 45 - 50%. This lack of sensitivity to σ indicates that in both cases there is sufficient time for the condensed phase mass to fall out before the Southern Hemisphere begins to warm from its wintertime minimum, so only a small amount of condensed phase mass is present to reevaporate as the vortex warms. The denitrification in the model Southern Hemisphere after winter is therefore determined primarily by the amount of HNO_3 removed from gas phase during winter, which is controlled by the minimum temperatures reached.

6.4. Dehydration

Dehydration of the polar vortex is also a consequence of the condensation and sedimentation of PSCs. Although the GMI model has a fixed background H_2O distribution, the PSC parameterization accounts for the loss of H_2O from the model due to sedimentation, as described in section 3.3.

Figure 9 shows the evolution of gas phase H_2O in the GMI model on the 47 hPa surface between June 15 and September 15. On June 15 there is no dehydration, which is consistent with the lack of Type 2 PSCs up to this day. Figure 9a also shows that the background H_2O distribution is longitudinally symmetric with typical values around 5 ppmv. By July 15, dehydration has begun in the GMI model, with minimum H_2O mixing ratios on the 47 hPa surface dipping below 3 ppmv. The most extensive dehydration occurs in August, with minimum H_2O mixing ratios below 1.5 ppmv. On September 15 the dehydration is nearly as extensive as that in the previous month, but the lowest values seen on August 15 have disappeared as the temperatures are rising and ice PSCs can no longer form.

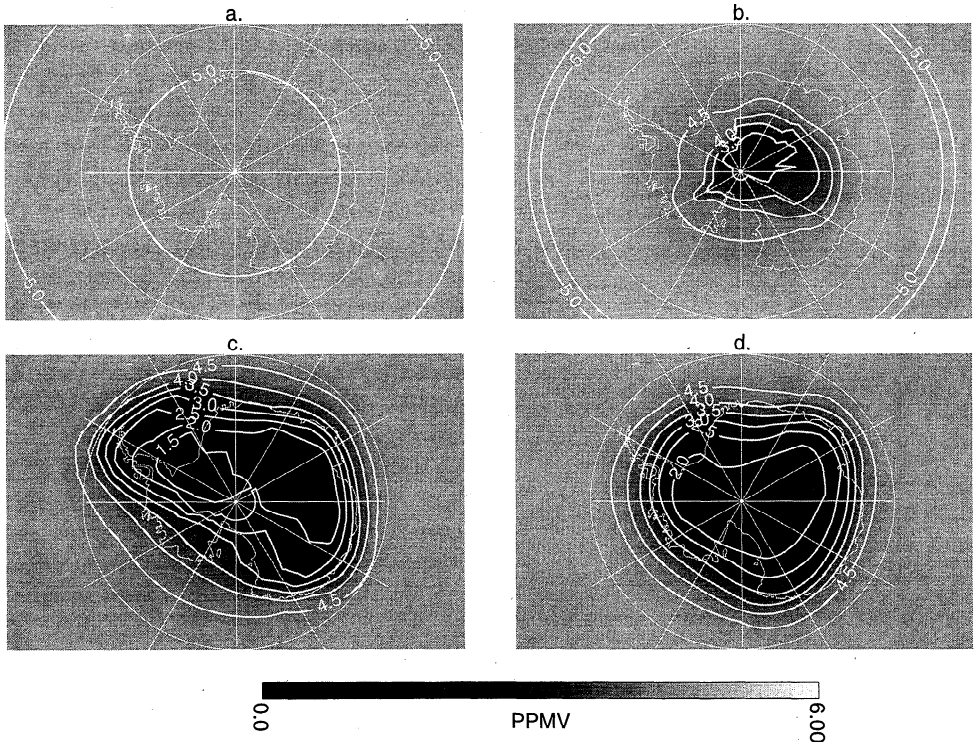

Figure 9. H_2O predicted by the GMI 3-D CTM at 47 hPa on (a) June 15, (b) July 15, (c) August 15, and (d) September 15. Units are parts per million by volume.

Figure 10 shows H_2O on the 46.4 hPa surface obtained from MLS version 3 observations in 1992 on June 15, July 12, August 18, and September 20. Figure 10 shows no evidence of significant dehydration on June 15, although CLAES 780 cm^{-1} extinction observations show that extensive PSC formation has occurred at this time [*Mergenthaler et al.,* 1997], and Figure 6 shows that the CLAES instrument also sees significant loss of HNO_3 from gas phase. This could occur if the PSCs forming in the atmosphere at that time do not contain significant amounts of H_2O.

On July 12 significant dehydration is evident, with minimum values reaching below 2.5 ppmv. The most extensive dehydration occurs in August, with minimum H_2O values reaching below 1 ppmv. At this time, the areal extents of the dehydration in the GMI model and the observations appear to agree reasonably well, although the comparison is hindered by the lack of observations south of -80°. On September 20 the observed H_2O distribution has increased significantly from the previous month. Minimum values are $\sim$ 3 ppmv. The GMI model appears to be more extensively dehydrated than is observed. Since all Type 2 PSCs have evaporated at this time, the GMI model may overestimate the amount of permanent dehydration resulting from condensation and sedimentation of PSCs.

Figure 11 compares normalized H_2O probability distributions for the GMI model and MLS observations constructed similarly to Figure 7. Figure 11b shows that in June all of the normalized H_2O values in the GMI model lie between 0.9 and 1.0, a consequence of the zonal symmetry of the background H_2O distribution, its weak meridional gradient at high latitudes, and the lack of PSC-induced dehydration. The larger observed variability of the June MLS probability distribution results from its longitudinal variability and perhaps a small amount of dehydration. In mid-July, $\sim$ 6% of the observed normalized H_2O values lie below 0.6, which is not captured by the GMI model. This is interesting because the mid-July HNO_3 distributions shown in Figure 7 compare relatively well at that time.

The lowest values of normalized H_2O occur in mid-August in both the model and the observations, with good agreement between the model and observed probability distributions. There is still a higher probability of finding low normalized H_2O values in the observations, with a 13% chance of observing normalized H_2O below 0.4 in contrast to an $\sim$ 8% chance in the model. In mid-September both the model and observed distributions show a reduced occurrence of the lowest normalized H_2O values, but in the observations there has been a larger reduction.

The November 1994 flight of ATMOS measured H_2O in addition to the NO_y species and N_2O discussed above. We can use these observations to construct H_2O^* and calculate the vortex-averaged residual dehydration in November for comparison with model results. This comparison is plotted in Figure 12. The agree-

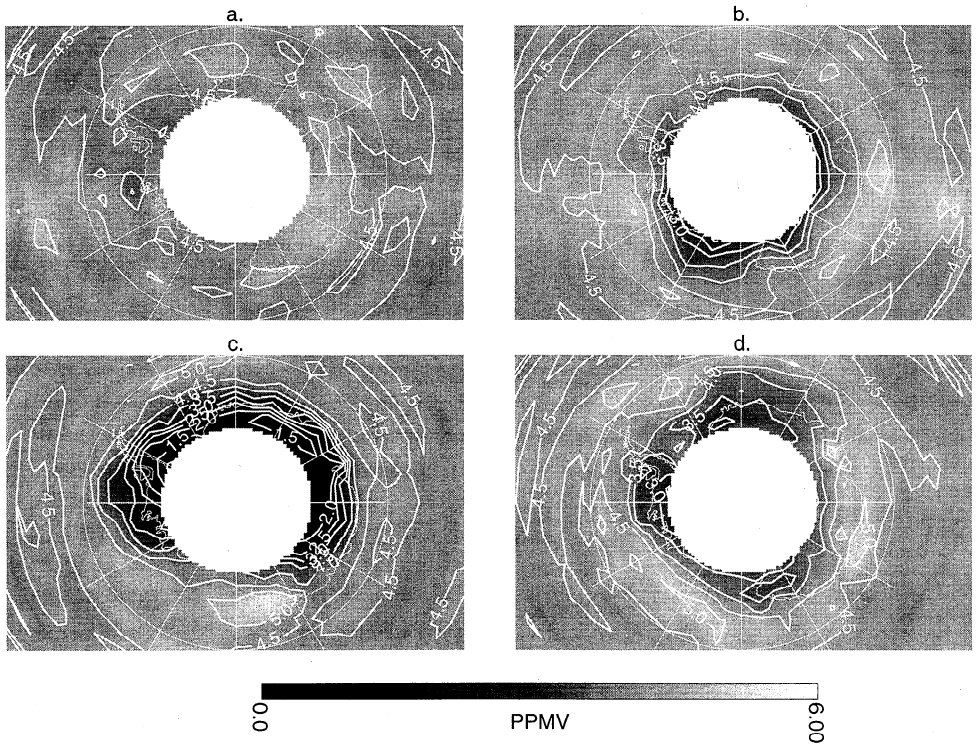

Figure 10. H_2O observed by the Microwave Limb Sounder (MLS) instrument on the 46.4 hPa surface on (a) June 15, (b) July 12, (c) August 18, and (d) September 20. Units are parts per million by volume.

ment between the modeled and observed dehydrations is very good, both in absolute (Figure 12a) and relative (Figure 12b) terms. The modeled peak dehydration occurs at nearly the same pressure level as that observed. Figure 12a indicates that the modeled dehydration is overestimated by $\sim$ 44% at 50 hPa, consistent with the dehydration overestimation suggested by Figure 11.

It is interesting to consider the observed denitrification of $\sim$ 60% seen at 40 hPa in Figure 8b and the observed dehydration of $\sim$ 10% at the same level in Figure 12b. This is a situation where the vortex denitrification is significant but dehydration is relatively small. A similar situation is seen in the GMI model at 30 hPa, where the model denitrification is $\sim$ 50% but dehydration is a little less than 10%. Two features of the model parameterization allow this large denitrification without large dehydration to occur: (1) The number density of the nucleating ice particles is small, resulting in large particles which fall rapidly, and (2) transfer of HNO_3 from the existing STS aerosol particles occurs rapidly enough so that the ice particles can carry significant amounts of HNO_3 out of the lower stratosphere with only a modest dehydration.

The evolution of gas phase H_2O through the winter and the dehydration of the Southern Hemisphere polar vortex in spring are similar in both the $\sigma = 1.6$ and $\sigma = 1.3$ runs. This is consistent with the behavior of HNO_3 and denitrification discussed in section 6.3.

7. Response to HSCT Emissions

In this section we examine the response of the Southern Hemisphere lower stratosphere to aircraft emissions of NO_x and H_2O. Figures 13a and 13b show the percentage change in vortex-averaged NO_y and H_2O, respectively, that occurs in the Southern Hemisphere polar vortex when stratospheric aircraft and their emissions are included in the year 2015 fleet assumption. In May, before any PSCs begin to form, NO_y increases range up to $\sim$ 3.5%, and H_2O increases peak at just over 3%.

The NO_y increases in May give way to small decreases in NO_y of up to 1.5% during July, August, and September, when both STS and ice PSCs are forming. NO_y decreases because additional H_2O from the HSCTs reduces equilibrium vapor pressures of HNO_3 over both Type 1 and Type 2 PSCs, moving more HNO_3 into condensed phase where it can sediment out of the atmosphere. Also, the addition of HSCT H_2O results in more frequent formation of ice PSCs which can carry more NO_y out of the vortex. The changes in H_2O shown in Figure 13b are never negative, but during the time and in the altitude range where ice PSCs are forming, increases in H_2O reach their smallest values.

Figures 14a and 14b show the percent change in vortex-averaged STS and ice SADs, respectively. Figure 14a shows that during most of the late fall and

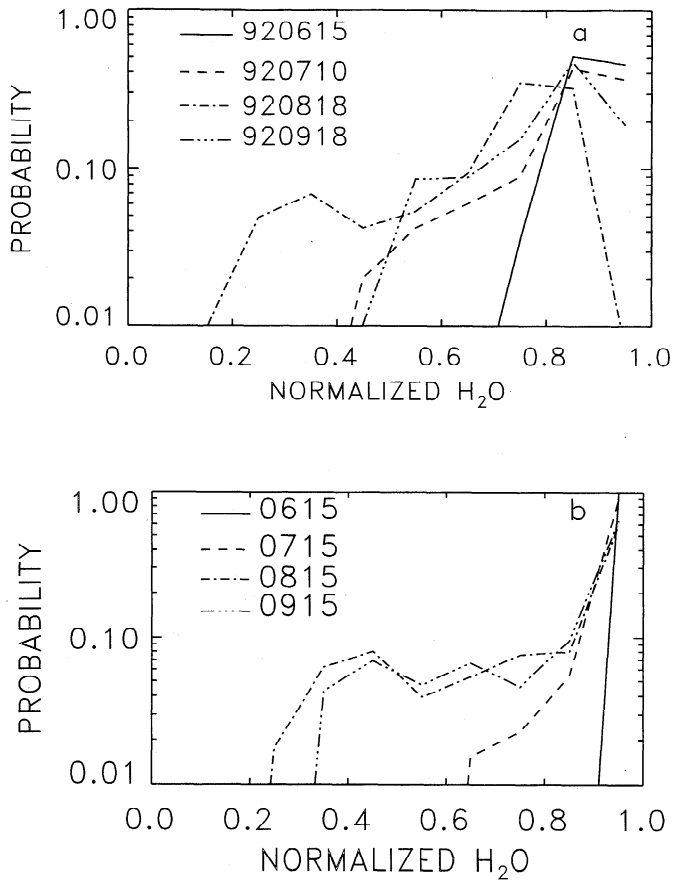

Figure 11. Normalized H_2O probability distributions constructed from (a) MLS H_2O observations and (b) values calculated by the GMI model. The distributions were constructed in the same manner as the HNO_3 probability distributions shown in Figure 7. The MLS distributions were constructed from retrievals taken on June 15, July 12, August 18, and September 20, 1992.

spring seasons, HSCT emissions increase STS SADs by up to 10%. During the summer in the lower stratosphere, ~ 5% decreases in STS SAD occur. These decreases probably result from the NO_y decreases shown in Figure 13a. Increases in STS SAD return later in the winter when the HSCT-induced changes to NO_y are again positive. Figure 14b shows that HSCT emissions typically increase the ice SADs by ~ 5 - 10%. There is also a small region in July at 40 hPa where ice SADs decrease. This may be because the H_2O increases in the HSCT-perturbed run trigger ice PSC formation earlier than in the subsonics-only run. If sedimentation subsequently removes enough ice SAD, when the PSCs form in the subsonics-only case the SAD will exceed the HSCT-perturbed SAD.

Changes in PSC formation will affect the concentration of active halogens in the model, and these in turn will affect O_3 concentrations. Figure 15a shows the percent change in active Cl_y (defined as for Figure 3a). Increases in active Cl_y are seen throughout the winter, with the peak increases of just over 5% occurring primarily in May and June when base active Cl_y values are ~ 30% of total Cl_y (Figure 3b). In absolute terms, peak increases also occur at this time. During the Southern Hemisphere springtime the increases are typically 1 - 3%. The effect of the aircraft emissions on vortex-averaged O_3 mixing ratios is shown in Figure 15b. Small decreases in O_3 concentrations occur throughout the altitude region, with peak decreases of ~ 1% between 30 and 50 hPa in October and November.

The importance of this result lies not in the particular predicted change in O_3 concentrations, which are small, but in the fact that we have attempted to account for all of the effects of PSCs in predicting it, including sedimentation. Sedimentation reduces PSC SADs in both the subsonics-only and HSCT-perturbed runs, which will result in a different change in the amount of Cl_y activation than would otherwise occur. Also, sedimentation-induced decreases in NO_y concentrations will reduce the rate of Cl_y deactivation in both the subsonics-only and HSCT-perturbed cases. Including the effects of sedimentation should therefore result in a more realistic prediction of the effects of HSCT emissions.

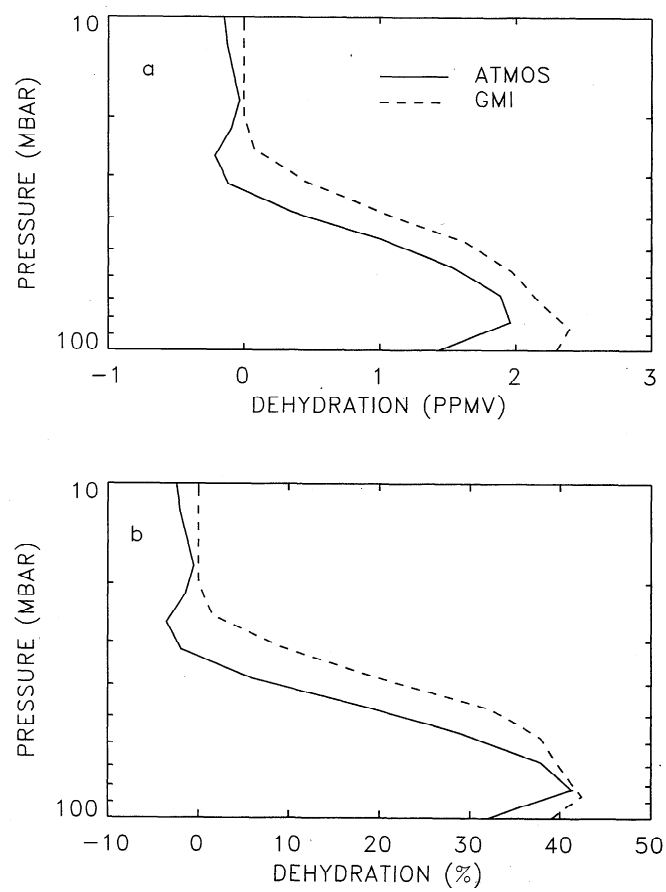

Figure 12. Vortex-averaged ΔH_2O (=H_2O^* − H_2O) in (a) parts per million by volume and (b) percentage. Plots are constructed from ATMOS observations of H_2O and N_2O (solid line) and GMI model output (dashed line.)

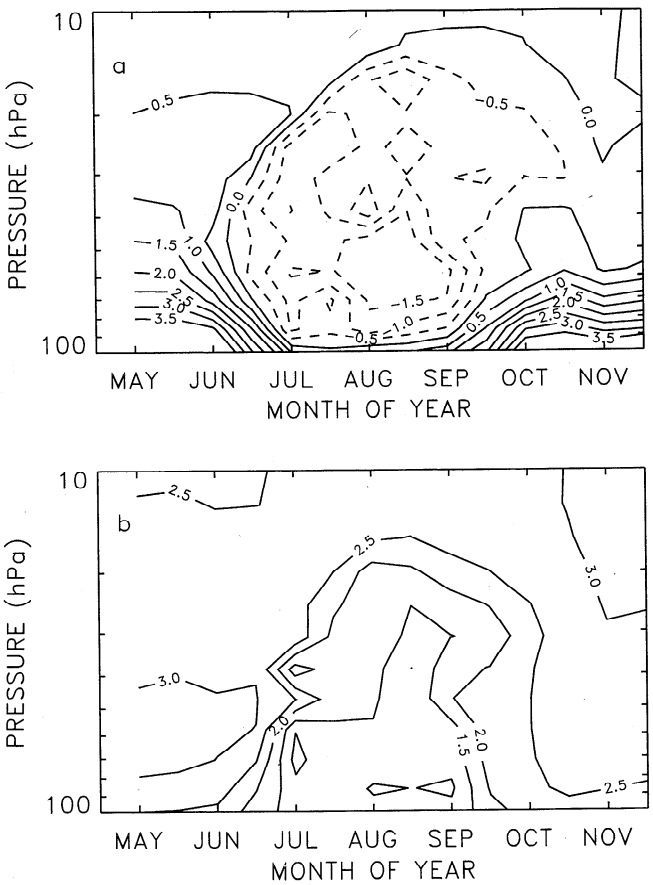

Figure 13. Changes in vortex-averaged NO_y and H_2O in the Southern Hemisphere due to the addition of high-speed civilian transport (HSCT) aircraft emissions. (a) Percent change in NO_y between May and November for pressure levels between 100 and 10 hPa. Solid contours show positive ΔNO_y regions, and dashed contours show negative ΔNO_y. (b) Percentage change in H_2O.

It is important to understand the sensitivity of the model response to HSCT emissions to changes in model and parameterization formulation. We therefore examined the model response to HSCTs for the $\sigma = 1.3$ case described in section 6. Although this change results in significantly larger PSC SADs, and $\sim$ 25% increases in gas phase NO_y and decreases in active Cl_y in the Southern Hemisphere lower stratospheric polar vortex during spring, the change in active Cl_y and O_3 from HSCT emissions is essentially the same as that of the standard run. This insensitivity increases our confidence in the predicted response to HSCTs.

Model deficiencies such as the phase lag between observed and predicted wintertime temperatures shown in Figure 1 and lower than observed HNO_3 concentrations (Figures 5 and 6) could also affect the predicted response to HSCTs. We feel that the temperature differences are unlikely to qualitatively change the model response. The largest temperature discrepancies between model and measurements occur early in the winter, when the model is warmer than observations. Colder temperatures would likely produce larger PSC surface area densities in the early part of the winter, but the reduced σ runs show that significant increases in PSC SADs do not change the amount of chlorine activation much during the spring. Also, because the model polar vortex is already significantly dehydrated and denitrified by the end of the winter, it is unlikely that colder temperatures early in the winter will produce significant additional denitrification and dehydration. The lack of sensitivity of chlorine activation, denitrification, and dehydration to changes in temperature should result in only small changes in the model response to HSCT emissions.

The effects of the low HNO_3 in the model are more difficult to determine. Model transport is likely to be responsible for much of the HNO_3 deficit, and a change in the model transport which increases HNO_3 in the polar lower stratosphere will also change the flux of HSCT emissions into the polar vortex. Addressing this question would require solving long-standing problems in

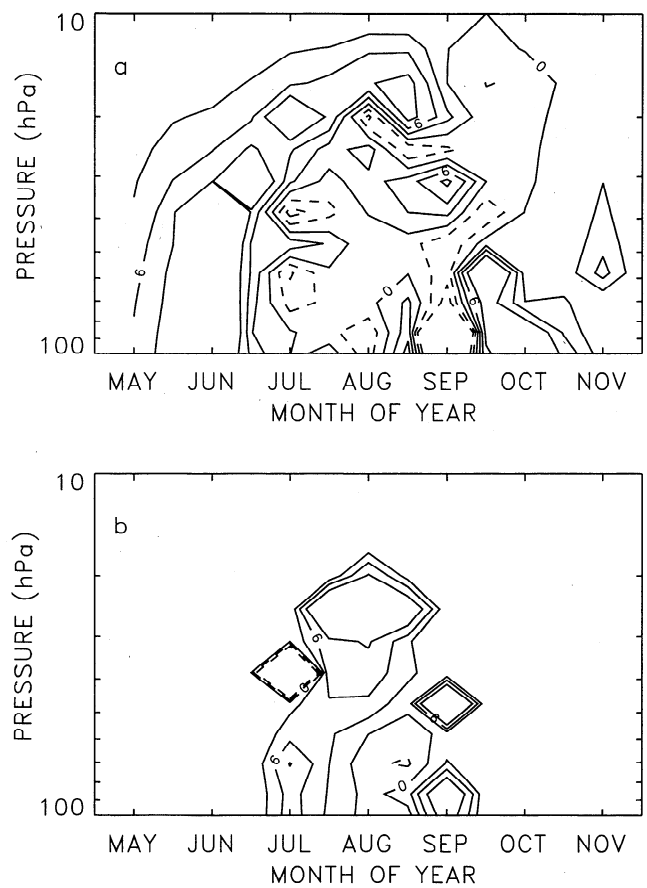

Figure 14. Percent changes in vortex-averaged STS and ice surface area densities, in the Southern Hemisphere due to the addition of HSCT aircraft emissions. (a) Percentage change in STS SAD between May and November for pressure levels between 100 and 10 hPa. Solid contours show positive ΔNO_y regions, and dashed contours show negative ΔNO_y. (b) Percent change in ice SAD. Contour levels are -6, -3, 0, 3, 6, and 10%.

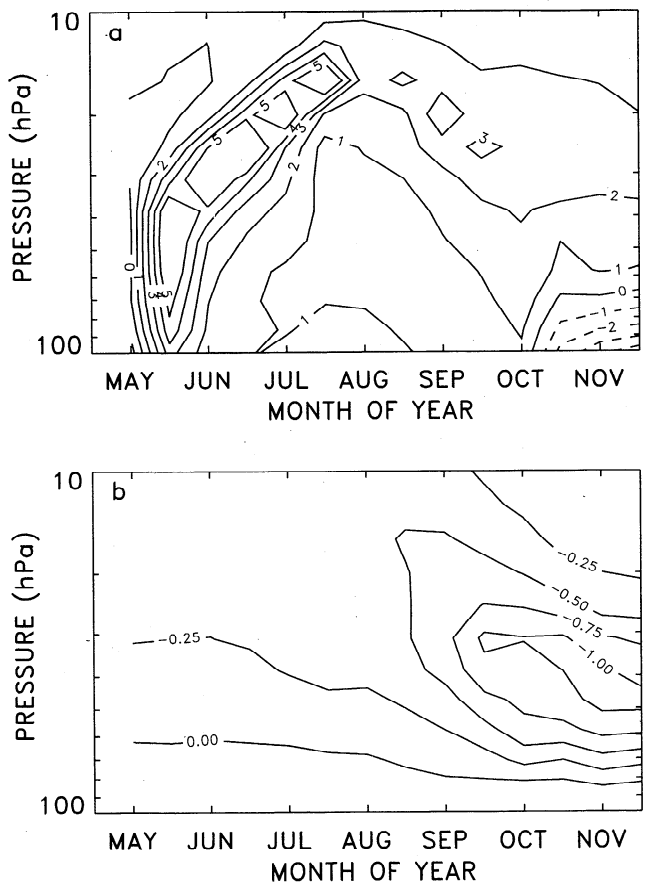

Figure 15. Changes in (a) vortex-averaged active Cl_y in parts per trillion by volume and (b) in vortex-averaged O_3 in percent. Values are for the Southern Hemisphere between May and November, for pressure levels between 100 and 10 hPa.

the modeling of atmospheric transport processes and is beyond the scope of this paper.

The HSCT emission scenario used in this study does not include HSCT emissions of H_2SO_4. These emissions can have a substantial impact on model predictions of global O_3 depletion due to HSCTs, because they substantially increase background sulfate aerosol SADs globally. If the emissions increase the number density of the background sulfate aerosol, they may produce increases in PSC surface area densities and polar O_3 depletion as well. However, the effects of HSCT emissions of H_2SO_4 on PSC size distributions and SADs are not currently well understood. Microphysical modeling of the PSCs is probably required and is beyond the scope of our current studies and this paper.

8. Summary and Conclusions

This paper has presented a PSC parameterization written for and implemented in the GMI 3-D CTM. The parameterization was designed to balance the need for physical realism with the computational constraints imposed by its intended use in 3-D model aircraft assessment studies.

The parameterization differs from more standard 3-D model PSC treatments such as that of *Chipperfield et al.* [1993] in the following ways: (1) An STS composition is assumed for Type 1 PSCs instead of NAT, (2) supersaturation ratios must be exceeded for solid phase aerosol formation to begin, (3) the number density of the aerosols is held constant instead of the particle radii, (4) the surface area densities are calculated assuming the aerosol particles are distributed lognormally, and (5) the sedimentation mass flux of the aerosols is consistent with the lognormal particle size distribution. With current settings the mass flux is close to a factor of 3 larger than it would be if all particles were assumed to have the same size.

Using the new GMI 3-D CTM with mixing ratio boundary conditions and background sulfate aerosol distributions corresponding to 1996 and winds and temperatures from the NCAR MACCM2′ general circulation model, we have examined the high-latitude Southern Hemisphere winter and spring simulation. The temperatures in the Northern Hemisphere are too warm for any significant PSC formation to occur. The Southern Hemisphere temperature distributions are similar to those observed in 1992 and 1994, although the coldest model temperatures lag those observed in the atmosphere in the early winter by 10 - 20 days.

Model-predicted surface area densities and particle sizes for Type 1 and Type 2 aerosols are consistent with in situ observations made from the ER-2 aircraft and lidar observations. PSC SADs are sufficient to activate a large fraction of the Cl_y in the polar vortex. This results in a well-developed and timed O_3 hole with minimum values reaching $\sim$ 120 DU in October.

In comparison with version 7 CLAES lower stratosphere HNO_3 retrievals, the GMI model exhibits a low bias in HNO_3. The bias results from an overall model underestimation of NO_y and a modeled HNO_3 profile which peaks at a higher than observed altitude. The GMI model captures relatively well the horizontal structure of HNO_3 seen in the CLAES observations and the time evolution through the winter and spring seasons of the low polar concentrations resulting from HNO_3 condensation into PSCs and subsequent loss through sedimentation. The early evolution of the low HNO_3 region is not captured well, because of warmer than observed model temperatures during the early winter.

Large denitrification of the Southern Hemisphere polar vortex occurs in the model. The model polar vortex denitrification occurring in mid-November compares well in the lower stratosphere with estimates of denitrification in the polar vortex made from ATMOS observations in early November to mid-November 1994. In absolute terms the model denitrification is significantly smaller than that observed, consistent with the overall low bias of NO_y in the model. Peak values of absolute denitrification are placed at $\sim$ 30 hPa in contrast to the observed peak at 50 - 60 hPa.

The evolution of polar H_2O concentrations over the

winter and early spring time period is reproduced relatively well in the model. The model early winter warm temperature bias results in an underestimation of the loss of gas phase H_2O, due to condensation of PSCs in the lower stratosphere. There is good model agreement with observations in August and a slight overestimation of the occurrence of low H_2O concentrations of gas phase H_2O in September.

The modeled dehydration of the Southern Hemisphere polar vortex compares very well in both relative and absolute terms with estimates of dehydration constructed from ATMOS observations. The shape of the model dehydration profile is in excellent agreement with the observed profile, while the magnitude of the dehydration is overestimated slightly. Peak dehydration in both the model and the observations occurs at $\sim$ 80 hPa, well below the observed (modeled) denitrification peak at 60 (30) hPa. The good reproduction of the observed dehydration profile demonstrates the feasibility of simulating PSC-induced dehydration in a model with a fixed background H_2O distribution.

As is seen in the observations, the model exhibits substantial denitrification in the polar vortex with small to modest dehydration. This is a consequence of the assumed small number of nucleated ice particles in comparison to the available condensation nuclei and the rapid transfer of HNO_3 from the STS aerosols to the ice aerosols when ice aerosols form.

HSCT emissions produce small increases ($\sim$3%) in NO_y and H_2O mixing ratios in the Southern Hemisphere polar vortex at the beginning of winter, resulting in an earlier occurrence of PSCs. Earlier onset of PSC sedimentation and lowered equilibrium vapor pressures of NO_y over STS and ice aerosols results in small decreases in NO_y ($\sim$ -1%) compared to the subsonics-only simulation later in the winter. H_2O mixing ratios at this time do not decrease, but show smaller increases than at the beginning of winter. Both ice and STS PSC SADs are larger than the subsonics-only simulation values at the beginning and end of winter, although during midwinter there are regions of the polar vortex where PSC SADs decline.

The HSCT emissions in the Southern Hemisphere polar vortex cause small increases in active Cl_y ($\sim$ 1%) during the Southern Hemisphere spring. The increased active Cl_y produces similarly small decreases in O_3 concentrations. Note that the chemical mechanism used in this study does not include a channel to HCl for the reaction of ClO and OH. *Lary et al.* [1995] show that this reaction will increase slightly the rate of Cl_y deactivation. Inclusion of this reaction in the model chemical mechanism should therefore reduce slightly the prediction of HSCT-induced O_3 depletion.

Future work involving this parameterization and model should focus on obtaining a meteorological data set with realistic Northern Hemisphere temperature distributions, establishing that this results in a realistic simulation of PSC occurrence and constituent evolution in the Northern Hemisphere, and determining the model predictions of the effects of HSCTs in the Northern Hemisphere. HSCT-induced changes in NO_y and H_2O in the Northern Hemisphere vortex are significantly larger than those in the Southern Hemisphere vortex, and the temperature structure is quite different. There is no reason to expect that the predicted impact of HSCTs in the Northern Hemisphere polar vortex will be as modest as is the case for the Southern Hemisphere. It is also important to further evaluate the effects of changes in the parameterization settings assumed in this study, such as the width of the particle size distributions, the neglect of NAT and STS PSC coexistence, and the assumed aerosol particle number densities.

Acknowledgments. The authors would like to thank J. Mergenthaler and J. Kumer for their suggestions regarding the CLAES data. This work was supported by the Atmospheric Effects of Stratospheric Aircraft component of the NASA Atmospheric Effects of Aviation Project and the NASA Upper Atmosphere Research Satellite mission.

References

Beyerle, G., B. Luo, R. Neuber, T. Peter, and I. S. McDermid, Temperature dependence of ternary solution particle volumes as observed by lidar in the Arctic stratosphere during winter 1992/1993, *J. Geophys. Res., 102*, 3606-3609, 1997.

Boville, B. A., Middle atmosphere version of CCM2 (MACCM2): Annual cycle and interannual variability, *J. Geophys. Res., 100*, 9017-9039, 1995.

Brasseur, G. P., X. X. Tie, P. J. Rasch, and F. Lefevre, A three-dimensional simulation of the Antarctic ozone hole: Impact of anthropogenic chlorine on the lower stratosphere and upper troposphere, *J. Geophys. Res., 102*, 8909-8930, 1997.

Carslaw, K. S., B. P. Luo, S. L. Clegg, T. Peter, P. Brimblecombe, and P. J. Crutzen, Stratospheric aerosol growth and HNO_3 gas phase depletion from coupled HNO_3 and water uptake by liquid particles, *Geophys. Res. Lett., 21*, 2479-2482, 1994.

Carslaw, K. S., B. Luo, and T. Peter, An analytic expression for the composition of aqueous HNO_3-H_2SO_4 stratospheric aerosols including gas phase removal of HNO_3, *Geophys. Res. Lett., 22*, 1877-1880, 1995.

Chipperfield, M. P., D. Cariolle, P. Simon, R. Ramaroson, and D. J. Lary, A three-dimensional modeling study of trace species in the arctic lower stratosphere during winter 1989 - 1990, *J. Geophys. Res., 98*, 7199-7218, 1993.

Considine, D. B., Signatures of high latitude dynamical processes and denitrification, in Models and Measurements II, edited by J. H. Park et al., Chap. 5.5, *NASA Tech. Memo, NASA TM-1999-209554*, 397 - 432, 1999.

Considine, D. B., A. R. Douglass, and C. H. Jackman, Effects of a polar stratospheric cloud parameterization on ozone depletion due to stratospheric aircraft in a two-dimensional model, *J. Geophys. Res., 99*, 18,879-18,894, 1994.

Del Negro, L. A., et al., Evaluating the role of NAT, NAD, and liquid $H_2SO_4/H_2O/HNO_3$ solutions in Antarctic polar stratospheric cloud aerosol: Observations and implications, *J. Geophys. Res., 102*, 13,255-13,282, 1997.

DeMore, W. B., D. M. Golden, R. F. Hampson, C. J. Howard, C. E. Kolb, M. J. Kurylo, M. J. Molina, A.

R. Ravishankara, and S. P. Sander, Chemical kinetics and photochemical data for use in stratospheric modeling, Evaluation number 12, *JPL Publ., 97-4*, 273 pp., 1997.

Dessler, A. E., J. Wu, M. L. Santee, and M. R. Schoeberl, Satellite observations of temporary and irreversible denitrification, *J. Geophys. Res., 104*, 13,993-14,002, 1999.

Douglass, A. R., M. M. Prather, T. M. Hall, S. E. Strahan, P. Rasch, L. Sparling, L. Coy, and J. M. Rodriguez, Choosing meteorological input for the global modeling initiative assessment of high-speed aircraft, *J. Geophys. Res.*, in press, 1999.

Drdla, K., A. Tabazadeh, R. P. Turco, M. Z. Jacobson, J. E. Dye, C. Twohy, and D. Baumgardner, Analysis of the physical state of one Arctic polar stratospheric cloud based on observations, *Geophys. Res. Lett., 21*, 2475-2478, 1994.

Dye, J. E., D. Baumgardner, B. W. Gandrud, S. R. Kawa, K. K. Kelly, M. Loewenstein, G. V. Ferry, K. R. Chan, and B. L. Gary, Particle size distributions in arctic polar stratospheric clouds, growth and freezing of sulfuric acid droplets, and implications for cloud formation, *J. Geophys. Res., 97*, 8015-8034, 1992.

Fahey, D. W., K. K. Kelly, G. V. Ferry, L. R. Poole, J. C. Wilson, D. M. Murphy, M. Loewenstein, and K. R. Chan, In situ measurements of total reactive nitrogen, total water, and aerosol in a polar stratospheric cloud in the Antarctic, *J. Geophys. Res., 94*, 11,299-11,315, 1989.

Gille, J. C., et al., Accuracy and precision of cryogenic limb array etalon spectrometer (CLAES) temperature retrievals, *J. Geophys. Res., 101*, 9583-9602, 1996.

Gobbi, G. P., G. Di Donfrancesco, and A. Adriani, Physical properties of stratospheric clouds during the Antarctic winter of 1995, *J. Geophys. Res., 103*, 10,859-10,873, 1998.

Granier, C., and G. Brasseur, Ozone and other trace gases in the Arctic and Antarctic regions: Three-dimensional model simulations, *J. Geophys. Res., 96*, 2995-3011, 1991.

Gunson, M. R., et al., The atmospheric trace molecule spectroscopy (ATMOS) experiment: Deployment on the ATLAS space shuttle missions, *Geophys. Res. Lett., 23*, 2333-2336, 1996.

Hanson, D., The uptake of HNO_3 onto ice, NAT, and frozen sulfuric acid, *Geophys. Res. Lett., 19*, 2063-2066, 1992.

Hanson, D., and K. Mauersberger, Laboratory studies of the nitric acid trihydrate: Implications for the south polar stratosphere, *Geophys. Res. Lett., 15*, 855-858, 1988.

Jackman, C. H., E. L. Fleming, S. Chandra, D. B. Considine, and J. E. Rosenfield, *J. Geophys. Res., 101*, 28,753-28,767, 1996.

Jacobson, M. Z., Computation of global photochemistry with SMVGEAR II, *Atmos. Environ., Part A, 29*, 2541-2546, 1995.

Kasten, F., Falling speed of aerosol particles, *J. Appl. Meteorol.*, 7, 944-947, 1968.

Kawa, S. R., et al., Assessment of the effects of high-speed aircraft on the stratosphere: 1998, *NASA Tech. Publ., TP 1999-209237*, 1999.

Kaye, J. A., and T. L. Miller, The ATLAS series of shuttle missions, *Geophys. Res. Lett., 23*, 2285-2288, 1996.

Koch, D., and D. Rind, $^{10}Be/^{7}Be$ as a tracer of stratospheric transport, *J. Geophys. Res., 103*, 3907-3917, 1998.

Kumer, J. B., et al., Comparison of correlative data with HNO_3 version 7 from the CLAES instrument deployed on the NASA Upper Atmosphere Research Satellite, *J. Geophys. Res., 101*, 9621-9656, 1996.

Lahoz, W. A., et al., Validation of UARS Microwave Limb Sounder 183 GHz H_2O measurements, *J. Geophys. Res., 101*, 10,129-10,150, 1996.

Larsen, N., Polar stratospheric clouds: A microphysical simulation model, *Rep. 91-2*, Dan. Meteorol. Inst., Copenhagen, 1991.

Lary, D. J., M. P. Chipperfield, and R. Toumi, The potential impact of the reaction $OH + ClO \rightarrow HCl + O_2$ on polar ozone photochemistry, *J. Atmos. Chem., 21*, 61-79, 1995.

Leu, M. T., Laboratory studies of sticking coefficients and heterogeneous reactions important in the Antarctic stratosphere, *Geophys. Res. Lett., 15*, 17-20, 1988.

Lin, S. J., and R. B. Rood, Multidimensional flux-form semi-Lagrangian transport schemes, *Mon. Weather Rev., 124*, 2046-2070, 1996.

Lipson, J. B., M. J. Elrod, T. W. Beiderhase, L. T. Molina, and M. J. Molina, Temperature dependence of the rate constant and branching ratio for the $OH + ClO$ reaction, *J. Chem. Soc. Faraday Trans., 93*, 2665-2673, 1997.

Manney, G. L., R. Swinbank, and A. O'Neill, Stratospheric meteorological conditions for the 3-12 Nov 1994 ATMOS/ATLAS-3 measurements, *Geophys. Res. Lett., 23*, 2409-2412, 1996.

Marti, J., and K. Mauersberger, A survey and new measurements of ice vapor pressure at temperatures between 170 and 250K, *Geophys. Res. Lett., 20*, 363-366, 1993.

Massie, S. T., et al., Simultaneous observations of polar stratospheric clouds and HNO_3 over Scandinavia in January, 1992, *Geophys. Res. Lett., 24*, 595-598, 1997.

Mergenthaler, J. L., J. B. Kumer, and A. E. Roche, Distribution of Antarctic polar stratospheric clouds as seen by the CLAES experiment, *J. Geophys. Res., 102*, 19,161-19,170, 1997.

Nash, E. R., P. A. Newman, J. E. Rosenfield, and M. R. Schoeberl, An objective determination of the polar vortex using Ertel's potential vorticity, *J. Geophys. Res., 101*, 9471-9478, 1996.

Peter, T., Microphysics and heterogeneous chemistry of polar stratospheric clouds, *Annu. Rev. Phys. Chem., 48*, 785-822, 1997.

Peter, T., C. Bruhl, and P. J. Crutzen, Increase in the PSC-formation probability caused by high-flying aircraft, *Geophys. Res. Lett., 18*, 1465-1468, 1991.

Pitari, G., V. Rizi, L. Ricciardulli, and G. Visconti, High-speed civil transport impact: Role of sulfate, nitric acid trihydrate, and ice aerosols studied with a two-dimensional model including aerosol physics, *J. Geophys. Res., 98*, 23,141-23,164, 1993.

Ramarosen, R., D. Pirre, and D. Cariolle, A box model for online computations of diurnal-variations in a 1-D model: Potential for application in multidimensional cases, *Ann. Geophys., 10*, 416-428, 1992.

Rinsland, C. P., et al., ATMOS measurements of $H_2O + 2CH_4$ and total reactive nitrogen in the November 1994 Antarctic stratosphere: Dehydration and denitrification in the vortex, *Geophys. Res. Lett., 23*, 2397-2400, 1996.

Roche, A. E., et al., Validation of CH_4 and N_2O measurements by the cryogenic limb array etalon spectrometer instrument on the Upper Atmosphere Research Satellite, *J. Geophys. Res., 101*, 9679-9710, 1996.

Rodriguez, J. M., Global modeling initiative, in Atmospheric Effects of Aviation: First Report of the Subsonic Assessment Project, Chap. 6, *NASA Ref. Publ., 1385*, 123-145, 1996.

Santee, M. L., A. Tabazadeh, G. L. Manney, R. J. Salawitch, L. Froidevaux, W. G. Read, and J. W. Waters, UARS Microwave Limb Sounder HNO_3 observations: Implications for Antarctic polar stratospheric clouds, *J. Geophys. Res., 103*, 13,285-13,313, 1998.

Schubert, S. D., R. B. Rood, and J. Pfaendtner, An assimilated data set for earth science applications, *Bull. Amer. Meteorol. Soc., 74*, 2331-2342, 1993.

Stolarski, R. S., et al., 1995 scientific assessment of the atmospheric effects of stratospheric aircraft, *NASA Ref. Publ.*, *1381*, 17-33, 1995.

Tabazadeh, A., O. B. Toon, and E. J. Jensen, Formation and implications of ice particle nucleation in the stratosphere, *Geophys. Res. Lett.*, *24*, 2007-2010, 1997.

Thomason, L. W., L. R. Poole, and T. Deshler, A global climatology of stratospheric aerosol surface area density deduced from stratospheric aerosol and gas experiment II measurements: 1984-1994, *J. Geophys. Res.*, *102*, 8967-8976, 1997.

Turco, R. P., O. B. Toon, and P. Hamill, Heterogeneous physicochemistry of the polar ozone hole, *J. Geophys. Res.*, *94*, 16,493-16,510, 1989.

Woodbridge, E. L. et al., Estimates of total organic and inorganic chlorine in the lower stratosphere from in situ and flask measurements during AASE II, *J. Geophys. Res.*, *100*, 3057-3064, 1995.

P. S. Connell and D. A. Rotman, Lawrence Livermore National Laboratory, Livermore, CA 94550.

D. B. Considine, Earth System Science Interdisciplinary Center, University of Maryland, College Park, MD 20742. (dbc@atmos.umd.edu)

A. R. Douglass, NASA Goddard Space Flight Center, Greenbelt, MD 20771.

D. E. Kinnison, National Center for Atmospheric Research, Boulder, CO 80307.

(Received March 31, 1999; revised July 30, 1999; accepted August 31, 1999.)